Nanoscale Advances

ROYAL SOCIETY OF CHEMISTRY

PAPER

View Article Online
View Journal | View Issue

Cite this: *Nanoscale Adv.*, 2025, **7**, 2634

Fn14-targeting, NIR-II responsive nanomaterials for enhanced radiotherapy against glioblastomas†

Wei Fu, ‡[ab] Qing Liang,‡[ab] Yuxi Ma,‡[ab] Shiqiong Lei,[c] Ruiqi Li, [ab] Xin Zheng,[ab] Lian Chen,[ab] Jiayuan Chen,[ab] Xing Cai,[ab] Xiaofang Dai,[ab] Hongwei Duan, [de] Wenshan He*[c] and Jinghua Ren *[abf]

Radiotherapy is a common treatment option for patients with glioblastoma multiforme. However, tumor heterogeneity causes varying responses to radiation among different tumor subpopulations. Cancer cells that endure radiotherapy exhibit radioresistance, resulting in the ineffectiveness of radiation therapy and eventual tumor relapse. In this study, we discovered that the fibroblast growth factor-inducible 14 (Fn14)-positive tumor cells were enriched in tumor residual foci after radiation, ultimately leading to treatment failure. Fn14-expressing glioma cells survived ionizing radiation through preferential activation of DNA damage checkpoint response. We have thus engineered an Fn14-targeting and NIR-II responsive plasmonic gold nanosystem named Fn14-AuNPs, which can precisely internalize into Fn14-overexpressed glioma cells and have an excellent BBB-crossing capability. As gold nanoparticles, by inhibition of DNA repair processes and induction of G_2/M cells cycle arrest, Fn14-AuNPs nanoparticles improved the radiosensitivity of tumor cells. Meanwhile, Fn14-AuNPs induced localized heat under NIR-II photoirradiation, thus impeding RT-induced DNA damage checkpoint response. This versatile nanosensitizer, combined with NIR-II laser photoirradiation, can eradicate radioresistant subpopulations of glioblastoma and improve the therapeutic effect of radiotherapy. This finding presents an effective radiosensitization strategy by targeting radioresistant subpopulations, which can efficiently overcome the constraints imposed in clinical radiotherapy and offer a hopeful avenue to enhance the treatment effectivity of radiotherapy in glioblastoma.

Received 20th September 2024
Accepted 1st March 2025

DOI: 10.1039/d4na00788c

rsc.li/nanoscale-advances

1. Introduction

Glioblastoma multiforme (GBM) is recognized as the most aggressive and primary malignant brain tumor in adult patients.[1,2] Despite undergoing standard-of-care therapies like surgery, radiotherapy, and chemotherapy, patients with GBM have a median overall survival of only 12 to 15 months, with a 5-year survival rate of merely 4.7%.[1–4] The restricted efficacy of current therapies is partially attributable to their heterogeneous nature.[5–9] GBM cells with distinct genotypes and phenotypes may harbor divergent signaling pathways in response to treatment, enabling certain cells to adapt and resist treatment. Rational therapeutic combinations based on an in-depth understanding of the relevant subpopulations associated with therapy resistance are potentially of great utility in glioma therapy.

Radiation therapy, as an integral component of GBM treatment, has been validated to enhance overall disease control.[10,11] Ionizing Radiation (IR) causes DNA damage through direct ionization and reactive oxygen molecular products, which in turn destroys tumor cells and impedes cell proliferation.[11] In spite of the progress made in modern radiation therapy techniques, local recurrence resulting from radiation-resistant tumor cells remains a barrier to the long-term survival of GBM patients.[12] Previous studies mainly ascribed the mechanism of radiation resistance to DNA damage repair and hypoxia.[13–15] Given that GBM is recognized as a highly heterogeneous disease, tumor cells with low radiosensitivity could potentially trigger local recurrence, ultimately resulting in the failure of radiotherapy.[16] Therefore, selectively eliminating the tumor cells with reduced radiosensitivity at conventional

[a]*Cancer Center, Union Hospital, Tongji Medical College, Huazhong University of Science and Technology, Wuhan 430022, China. E-mail: jhrenmed@hust.edu.cn*
[b]*Hubei Key Laboratory of Precision Radiation Oncology, Wuhan 430022, China*
[c]*Department of Breast and Thyroid Surgery, Union Hospital, Tongji Medical College, Huazhong University of Science and Technology, Wuhan 430022, China. E-mail: hewenshan@hust.edu.cn*
[d]*School of Chemical and Biomedical Engineering, Nanyang Technological University, Singapore 637457, Singapore*
[e]*Lee Kong Chian School of Medicine, Nanyang Technological University, Singapore 636921, Singapore*
[f]*Shenzhen Huazhong University of Science and Technology Research Institute, Shenzhen 518057, China*

† Electronic supplementary information (ESI) available: Access the Web version on PubMed Central for supplementary resources. See DOI: https://doi.org/10.1039/d4na00788c

‡ Wei Fu, Qing Liang and Yuxi Ma contributed equally to this work.

radiation therapy doses could be crucial in overcoming the resurgence of GBM.

In this study, we found that high expression of fibroblast growth factor-inducible 14 (Fn14) in glioblastoma tissue was associated with poor progression-free survival (PFS) using the datasets of the Cancer Genome Atlas (TCGA). Fn14, also known as TNFRSF12A, has been identified as a member of the tumor necrosis factor receptor superfamily. It is a type I transmembrane protein composed of 129 amino acid residues.[17–19] The binding of Fn14 with its ligand TWEAK may facilitate cellular activities including proliferation, invasion, angiogenesis and inflammation. Here, we showed that the $Fn14^+$ subpopulation in glioblastoma was resistant to radiotherapy by preferential activation of DNA damage checkpoint response and induction of G_2/M cells. Our results further demonstrated that mild hyperthermia hindered DNA damage repair. Thus, we speculated that mild hyperthermia in combination with radiotherapy may represent a therapeutic approach for GBM through targeting $Fn14^+$ cells.

Previous studies have shown that nanoparticles can enhance the radiosensitivity of tumor cells by several crucial processes, including enzyme-like catalytic activity, the production of reactive oxygen species (ROS), induction of cell cycle arrest, disruption of radiation-induced DNA damage repair, and inhibition of hypoxia.[20,21] Here, we constructed the Fn14-targeting and near-infrared (NIR)-II-activated nanosystem that can sensitize the Fn14-positive GBM cells to radiotherapy through impairment of DNA repair and induction of cell-cycle arrest. In line with our previous work,[22] we synthesized plasmonic gold nanoparticles (AuNPs) using a tailored approach involving the dopamine-mediated reduction of gold precursors. Delivering nanoparticles to the brain is challenging owing to the existence of the blood–brain barrier (BBB).[23] Under normal physiological conditions, substances can pass through the BBB by: (i) passive diffusion, (ii) transport *via* carriers, (iii) transcytosis mediated by adsorption, (iv) transport mediated by receptors, and (v) efflux pumps. A previous study showed that AuNPs can traverse the BBB *via* passive diffusion, owing to their small size (≤60 nm).[24] Therefore, AuNPs have an excellent capacity to penetrate the BBB. Besides, the hyperbranched AuNPs exhibit localized surface plasmon resonance (LSPR) across a wide range of wavelengths, extending from the visible to the NIR spectral range. Upon the attachment of the D-enantiomeric peptide ligand to Fn14, AuNPs transform into the photonic and Fn14-targeting nanomaterial, Fn14-AuNPs. Relying on the disruption of DNA repair pathways, the increase of G_2/M cells and its NIR-II photothermal effect, Fn14-AuNPs enhanced the radiation damage effect under conventional radiation doses on GBM and selectively eliminate tumor cells in residual GBM sites, striving to suppress tumor development and prolong its long-term survival.

2. Experimental section

2.1 Reagents and antibodies

The enantiomeric peptide ligand of Fn14 (D-FNB, sequenced as $^{D}C^{D}H^{D}P^{D}R^{D}E^{D}V^{D}D^{D}V^{D}E^{D}L^{D}Y^{D}S^{D}T^{D}V^{D}F^{D}G^{D}H$) was synthesized by Bankpeptide (Hefei, China). In this research, multiple primary antibodies were applied, including anti-γ-H2AX (rabbit, 1 : 5000, Abcam, ab81299), anti-CD266 (Fn14, TWEAK Receptor) monoclonal antibody (ITEM-4) (mouse, 1 : 250, Abcam, ab109365), anti-AKT monoclonal antibody (rabbit, 1 : 1000, Abcam, ab314110), anti-phospho-AKT (Ser473) monoclonal antibody (rabbit, 1 : 1000, Abcam, ab81283), anti-PI3 Kinase p110 beta monoclonal antibody (rabbit, 1 : 1000, Abcam, ab302958), anti-DNA-PKcs polyclonal antibody (rabbit, 1 : 1000, Sigma, SAB4502385), anti-phospho-DNA-PKcs (Ser2056) polyclonal antibody (rabbit, 1 : 1000, Sigma, SAB4504169) and anti-GAPDH (rabbit, 1 : 5000, Abcam, ab8245).

2.2 Synthesis of Fn14-AuNPs

Synthesis of Fn14-AuNPs was schematically shown in Fig. 2a. Briefly, 1.8 ml dopamine at 4 mg ml^{-1} was incorporated into a mixture containing 27 ml Tris/HCl buffer (pH 8.5, 10 mM), 6 ml H_2O, 0.9 ml PVP (2 mg ml^{-1}, 10 kD) and 3 ml ethanol. Before adding 379 μl of HAuCl4 (24.085 mM), the mixture was stirred forcefully for 3 minutes. Then, the supernatant was abandoned and 3 ml bicine buffer (pH 8.5, 10 mM) was added to the rest. Next, 150 μl NH_2-PEG-NH_2 (5kD, 10 mg ml^{-1}) was incorporated to react with succinimidyl 4-(*N*-maleimidomethyl) cyclohexane-1-carboxylate through sustainably stirring for 24 h under room temperature, which further connected to polypeptide D-FNB with cysteine terminal. After centrifugation (8000 rcf) for 5 min, the precipitation was dispersed to PBS.

2.3 The TCGA analysis

From the TCGA database, 153 tumor samples in the glioblastoma datasets were obtained, accessible *via* **https://portal.gdc.cancer.gov/repository**. The obtained datasets were converted into transcripts per million values. Survival analyses were performed by the Cox proportional-hazards model. The hazard ratio was assessed relative to the lowest-risk group using a two-sided Wald test. The split Fn14 expression among GBM patients was established at 20%, with PFS ranging from 0 to 50 months and disease-specific survival (DSS) spanning 0 to 80 months.

2.4 Cell culture and viability assay

The glioblastoma-derived human cell (U251 cell) was sourced from the National Collection of Authenticated Cell Cultures in Shanghai, China. The mouse-derived microglial cell (BV2 cell) was provided by Xiaorong Dong from Huazhong University of Science and Technology. The brain-derived endothelialcell.3 (bEnd.3 cell) was purchased from National Collection of Authenticated Cell Cultures (JSCALL, Shanghai, JSY-CC1889). As described previously, Fn14 overexpression ($Fn14^{OE}$) U251 cells were constructed by using the lentiviral system.[25] Cells were cultured with DMEM (GIBCO, USA) containing 10% fetal bovine serum (GIBCO, USA) and 5% streptomycin/penicillin, and maintained at 37 °C in a 5% CO_2 atmosphere. Cell proliferation was evaluated by using Cell Counting Kit-8 (Beyotime, C0037, China). Cells were seeded at a density of 6×10^3 in 96-well plates and cultured for 24, 48, and 72 h respectively.

Subsequently, 8 μl per well assay solution was added to 96 well, then incubated for 1 h. The measurement of absorbance at 450 nm was carried out using a Multimode Plate Reader (EnSpire® 2300, USA).

2.5 Western blot analysis

Protein was extracted from U251 or Fn14^{OE} U251 cells with RIPA buffer (Beyotime, P0013B) and separated by 10% SDS-PAGE gels. Subsequently, the protein-containing gels were transferred to polyvinylidene difluoride (PVDF, Bio-rad) membranes. Primary antibodies were mentioned below: anti-CD266 (Fn14, 1 : 250), anti-AKT (1 : 1000), anti-phospho-AKT (Ser473) (1 : 1000), anti-PI3K (1 : 1000), anti-DNA-PKcs (1 : 1000), anti-phospho-DNA-PKcs (Ser2056) (1 : 1000) and anti-GAPDH (1 : 5000).

2.6 Colony formation assay

U251-parental or U251-Fn14^{OE} cells were planted in six-well plates at densities of 500, 1000, 2000, 4000, and 6000 per well, and then exposed to irradiation at doses of 0, 2, 4, 6, and 8 Gy using 6 MV X-rays at a rate of 600 cGy min^{-1} with the Trilogy System Linear Accelerator. After being exposed to IR, cells were cultured for approximately two weeks. Then, the cells were fixed using 4% paraformaldehyde (Beyotime, P0099) and stained using the crystal violet staining solution (Beyotime, C0121). The colonies with more than 50 cells were counted. Plating efficiency (%) = (number of colonies formed/number of cells plated) × 100. As previously described,[26] the single-hit multi-target model was applied to compute the surviving fraction. To confirm the repeatability of the experiment, we verified our findings through three separate experiments.

2.7 γ-H2AX assay

Cells were fixed using 4% paraformaldehyde, permeabilized using 0.2% Triton X-100 (Beyotime, P0096) and blocked using 5% BSA (Beyotime, ST023) at 0.5, 4 and 24 h after irradiation, respectively. The cells were then incubated overnight at 4 °C with anti-γ-H2AX (rabbit, Abcam, ab81299, 1 : 5000). The following day, cells were treated with a fluorescent secondary antibody (Abcam, ab150083, 1 : 1000) and subsequently stained with DAPI (1 mg ml^{-1}) (Beyotime, C1005). γ-H2AX foci were detected using an excitation wavelength of 652 nm and an emission wavelength of 668 nm. In addition, images were captured at a high magnification (63× objective) with a laser confocal microscope (Nikon EZ-C1 Si, Japan). To define a focus and filter out noise, we established a brightness threshold of 100/255 on the original image, and the minimum spot size was set to 7 pixels. The quantifications of mean γ-H2AX foci numbers per cell were estimated from 3 different fields of view.

2.8 Real-time quantitative polymerase chain reaction (qRT-PCR)

To investigate the possibility that irradiation may upregulate the expression of Fn14 in GBM cells, U251 cells at a density of 0.5 × 10^5 per well were planted in six-well plates and cultured overnight and physically irradiated at 5, 10 Gy. Then, total RNA was isolated from cells on days 5 and 10 after irradiation *via* the RNA Extraction Kit (Omega, USA). The total RNA was subsequently reverse-transcribed into cDNA through HiScript III-RT SuperMix (Vazyme, China). qRT-PCR was conducted using ChamQ SYBR qPCR Master Mix (Vazyme, China). By the ΔΔCt method, the relative levels of mRNA for the target gene were computed. The primers for Fn14 are: sense 5′-CCA AGC TCC TCC AAC CAC AA-3′ and anti-sense 5′-TGG GGC CTA GTG TCA AGT CT-3′. GAPDH primers: sense strand 5′-ATC CCA TCA CCA TCT TCC-3′, anti-sense strand 5′-ATG ACC CTT TTG GCT CCC-3′.

2.9 Cytotoxicity measurement

To enable cell attachment, Fn14^{OE} U251 cells (2 × 10^5 per well) were planted onto a 24-well micro-plate overnight. Subsequently, the initial culture media was substituted with fresh DMEM solutions containing Fn14-AuNPs (150 μg ml^{-1}). The next day, cells were then separately irradiated *via* a 1064 nm laser (0.33 W cm^{-2}, 15 min, controlled temperature at about 42.5 °C and 48 °C). To visually observe the killing effects, cells were stained with the live/dead staining kit (Beyotime, C2030S) for 30 min, washed with PBS three times and then imaged using a laser confocal microscope.

2.10 Cell cycle analysis

Fn14^{OE} U251 cells were treated with Fn14-AuNPs (150 μg ml^{-1}) for 24 h, followed by exposure to 4 Gy irradiation. The following day, the cells were fixed using 4% polyformaldehyde and stained using propidium iodide (20 μg ml^{-1}) containing RNase A (0.2 mg ml^{-1}) and 0.1% Triton X-100. Cell cycle analysis was conducted using FACS. ModFit LT software was utilized for analyzing the acquired data.

2.11 *In vitro* BBB permeability analyses

In vitro BBB models were established using a 24-well transwell culture system as previously described.[27] Briefly, bEnd.3 cells (1 × 10^5 per well) were seeded in the upper chamber with a pore diameter of 0.4 μm. The cells were cultured for 7–9 days to form an intact monolayer. The integrity of the BBB model was monitored by measuring transendothelial or transepithelial electrical resistance (TEER). Fn14^{OE} glioma cells (5 × 10^4 per well) were seeded in the lower chamber one day before Fn14-AuNPs treatment. Subsequently, 100 μl (150 μg ml^{-1}) AuNPs and Fn14-AuNPs were added to the apical upper chambers of the BBB models. Approximately 6 h after incubation, cells from lower chamber were detached from each well with trypsin and collected. The penetration across BBB and cellular uptake of Fn14-AuNPs were measured by transmission electron microscopy and inductively coupled plasma mass spectrometry (ICP-MS) analysis. For ICP-MS analysis, the trypsinized cells were then digested separately with aqua regia and analyzed for Au content.

2.12 The biodistribution and biosafety evaluation of nanoparticles

AuPB (100 μl per mouse, 150 μg ml^{-1}) and Fn14-AuPB (100 μl per mouse, 150 μg ml^{-1}) were intravenously injected into the orthotopic U251-bearing BALB/c nude mice. Major organs, including the heart, spleen, liver, lung, kidney and cancerous brain, were collected at 24 h post-injection. ICP-MS was conducted to quantify the Au content of different organs. To validate the retention ability of Fn14-AuPB *in vivo*, we also injected AuPB (100 μl per mouse, 150 μg ml^{-1}) and Fn14-AuPB (100 μl per mouse, 150 μg ml^{-1}) through the tail vein on orthotopic U251 GBM-bearing mice. We collected their tumor tissues for ICP-MS analysis on days 1, 5, 10 and 15 after Fn14-AuPB injection.

To assess the biosafety of Fn14-AuPB for their potential application *in vivo*, the injection of PBS, AuPB (100 μl per mouse, 150 μg ml^{-1}) and Fn14-AuPB (100 μl per mouse, 150 μg ml^{-1}) was conducted through the tail vein. The weights of mice were recorded every two days after intravenous injection. Moreover, after 14 days, mice were sacrificed for blood biochemistry, blood routine tests and histology analysis of major organs like the heart, spleen, liver, lung, kidney and brain *via* H&E staining. The serum, which was separated from blood samples by centrifuging at 1000 rcf for 10 min, was used for the blood biochemistry analysis for alanine aminotransferase (ALT), aspartate aminotransferase (AST), blood urea nitrogen (BUN) and creatine (CR). The whole blood was used for blood routine examination.

2.13 Tumor models and treatment

Female BALB/c nude mice with 5–6 weeks, were sourced from Changzhou Cavens Laboratory Animal Co., Ltd. The protocol for the animal study received approval from the Animal Ethics Committee at Huazhong University of Science and Technology (IACUC Number 3066). To construct the orthotopic U251-Luc or $Fn14^{OE}$ U251-Luc glioblastoma tumor-bearing mice models, 8 μl PBS containing 5×10^5 cancer cells was delivered into the mice's right caudate nucleus. Afterward, the tumor growth in mice was observed through bioluminescence imaging (Bruker, Ettlingen, Germany).

For *in vivo* therapy, the mice were anesthetized intraperitoneally (xylazine 7.5 mg kg^{-1} + zoletil 40 mg kg^{-1}) and injected intravenously with AuNPs or Fn14-AuNPs (150 μg ml^{-1}) at day 20 after tumor inoculation. NIR-II irradiation (0.33 W cm^{-2}, 6 min) was given on days 21, 22, 23, 24 and 25 after implantation. In the X-ray irradiation groups, mice were exposed to whole brain irradiation (2 Gy) within 10 min after mild photothermal therapy. Fractionated radiotherapy (10 Gy in total, 2 Gy per day for 5 days) was given on days 21, 22, 23, 24 and 25 after tumor implantation *via* 6 MV X-rays (source skin distance: 100 cm; radiation field: 40×4 cm; 600 cGy min^{-1}, Trilogy System Linear Accelerator). The progression of GBM was monitored by bioluminescent imaging (intraperitoneal injection of 20 mg per ml D-luciferin) *via in vivo* MS FX PRO Imager. The mice were followed for survival and euthanized when neurological symptoms became evident, as described previously.[28–30]

2.14 Tissue immunohistochemical (IHC) and immunofluorescence staining

Histopathology test using Hematoxylin and Eosin Staining Kit (H&E staining Kit, Beyotime, C0105) staining was conducted on the heart, liver, kidney, brain, spleen and lung tissues of treated mice, as previously described.[31] Murine glioma specimens for immunofluorescence on histological sections were fixed in 4% paraformaldehyde, permeabilized with 0.2% Triton X-100, and blocked with 5% BSA. Then the specimens were incubated with anti-mouse CD266 (1 : 100 dilution in 0.5% BSA/PBS) at 4 °C overnight while avoiding drying. Sections were washed three times using PBS, and followed by the application of secondary fluorescent antibodies. The slides were subjected to three PBS washes, stained with 200 μl of DAPI (1 mg ml^{-1}) for 15 minutes and observed through a confocal microscope (Nikon EZ-C1 Si, Japan). The images of the slices were taken *via* the Image-Pro Plus 6.0.

2.15 Statistical analysis

Each experiment was conducted three times. The data were presented as the standard error of the mean (SEM) or as the mean ± standard deviation (SD). A one-way ANOVA was employed for multiple comparisons, while the chi-square test was utilized for analyzing clinical characteristics. Statistical significance was established at $*p < 0.05$, $**p < 0.01$, $***p < 0.001$ and $****p < 0.0001$.

3. Results and discussion

3.1 Synthesis and characterization of Fn14-AuNPs

Tumor heterogeneity is a substantial obstacle in traditional GBM treatment including radiotherapy.[16] Thus, identifying and targeting glioma cell subpopulations associated with radioresistance can help improve the efficacy of radiotherapy in GBM. By analyzing the TCGA database of GBM patients, we discovered that high Fn14 expression group ($Fn14^{hi}$ group) had shorter PFS and DSS in GBM patients, compared with low expression group ($Fn14^{lo}$ group) (PFS:$Fn14^{hi}$ 5.03 months *vs.* $Fn14^{lo}$ 7.97 months, $p = 0.034$; DSS:$Fn14^{hi}$ 14.2 months *vs.* $Fn14^{lo}$ 16 months, $p = 0.046$) (Fig. S1a and b†). Together, these results suggested that elevated Fn14 expression was correlated with poor clinical outcomes in GBM patients. Fn14, part of the tumor necrosis factor receptor (TNFR) superfamily, is involved in tumor growth and treatment resistance.[32–35] To explore the role of Fn14 in GBM radiotherapy, we overexpressed Fn14 ($Fn14^{OE}$) in GBM U251 cells (Fig. 1a) and evaluated whether its overexpression enhanced the proliferation capacity of cells. The CCK-8 assay results displayed that there was no notable difference between the Ctrl and $Fn14^{OE}$ groups, indicating that Fn14 overexpression in GBM cells did not intensify cell proliferative capacity (Fig. S1c†). Subsequently, we employed colony formation assays to assess the reproductive death of glioma with different Fn14 expressions after treatment with IR. $Fn14^{OE}$ glioma cells were more resistant to IR treatment than their parental cells (Fig. 1b). To further elucidate the mechanism behind the survival of $Fn14^{OE}$ glioma cells, we investigated the

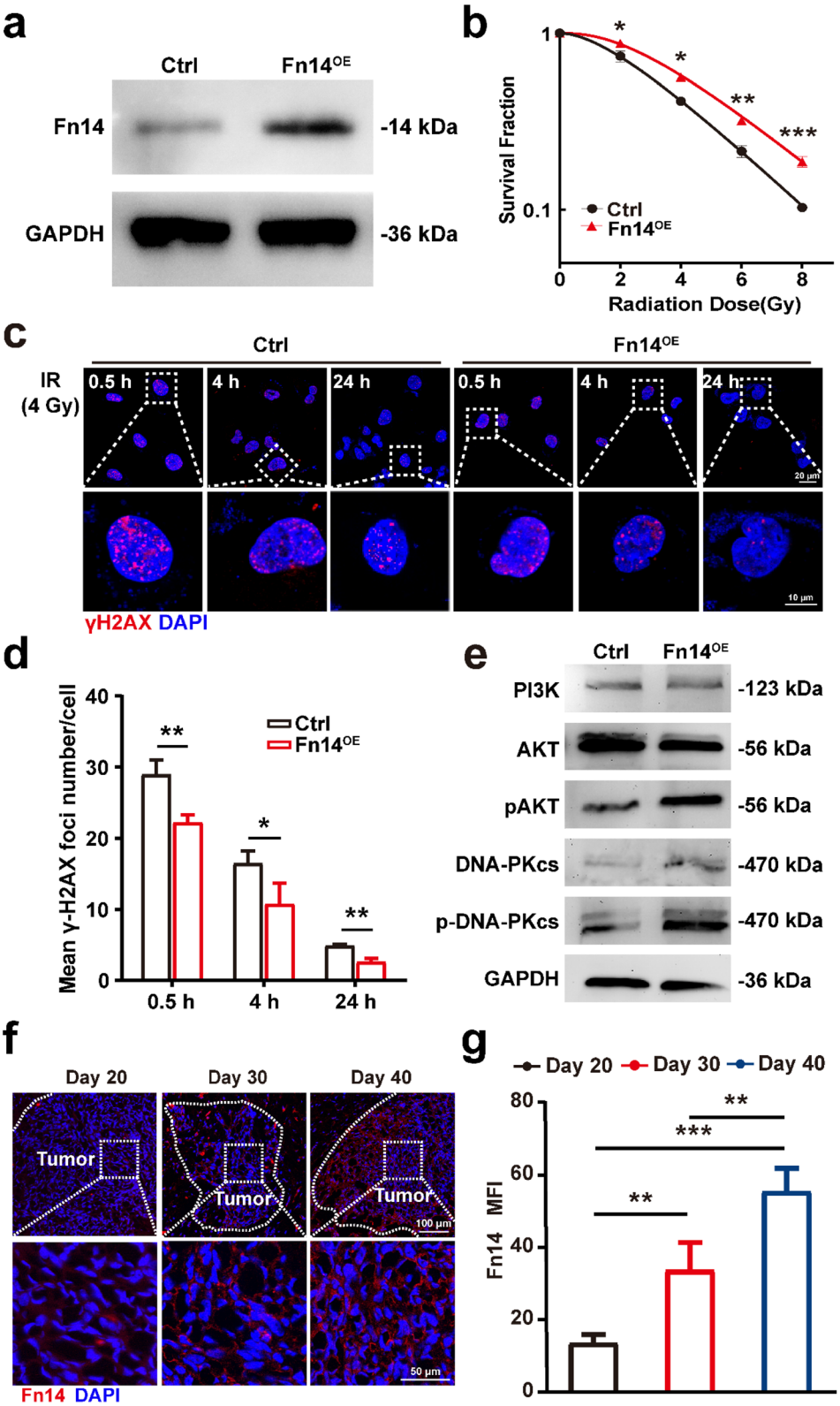

Fig. 1 High expression of Fn14 is correlated with radioresistance in glioblastoma. (a) Western blot for total Fn14 in U251 cells and Fn14^{OE} U251 cells. (b) Clonogenic cell survival curve of U251 cells and Fn14^{OE} U251 cells following different doses of radiation. (c) and (d) Fluorescence staining images and quantification of γ-H2AX foci in U251 cells and Fn14^{OE} U251 cells under radiation (IR: 4 Gy) (Scale bar: 20 μm (upper row) and 10 μm (lower row). (e) Western blot analysis of PI3K, AKT, p-AKT, DNA-PKcs and p-DNA-PKcs in U251 cells and Fn14^{OE} U251 cells after irradiation (IR: 4 Gy). (f) Fluorescence staining images of Fn14 in the brain tissues from irradiated-mice at different time points (day 20, 30 and 40 post-implantation of GBM; scale bar: 100 μm and 50 μm). (g) The mean fluorescence intensity of Fn14 was measured. Data are presented as mean ± SD, with $n = 3$ per group. Statistical significance is indicated as follows: *$p < 0.05$, **$p < 0.01$, ***$p < 0.001$.

DNA damage dynamics of glioma cells in response to irradiation by γ-H2AX foci assay.[36] The γ-H2AX foci assay revealed that the basal level of γ-H2AX foci in Fn14^{OE} glioma cells was lower than their parental U251 cells (Fig. 1c and d), which suggested a blunted early response to the induction of DNA double-strand breaks (DSBs). It should be noted that an accelerated descent of γ-H2AX foci in Fn14^{OE} glioma cells in the subsequent post-incubation period (up to 24 h). In contrast, the sustained presence of γ-H2AX foci in parental U251 cells following irradiation indicated that these cells were relatively sensitive to DNA damage.

Previous evidence suggested that Fn14 positively correlated with the activation of AKT signaling in GBM specimens.[37] Moreover, the abnormal activation of the AKT signaling can promote DNA DSB repair, leading to the enhanced radioresistance of GBM cells.[38] Hence, we hypothesized that Fn14 reduced the radiosensitivity of GBM cells by aberrant AKT signaling activation. Consistent with our hypothesis, expression levels of both phosphorylated AKT (p-AKT) and phosphorylated DNA-PKcs (p-DNA-PKcs) were elevated in Fn14^{OE} U251 compared to those in parental U251 cells (Fig. 1e). It is likely that Fn14 overexpression could aberrantly activate DNA damage checkpoint response, resulting in radioresistance of GBM. To explore the dynamics of tumor size with different Fn14 expression in response to irradiation, we constructed orthotopic xenograft GBM mice models by intracranially injecting a 9 : 1 mixture of U251-parental and U251-Fn14^{OE} cells (Fig. S1d†). The tumor-bearing mice underwent fractionated radiotherapy (10 Gy in 5 fractions). Bioluminescent imaging demonstrated a substantial reduction in tumor size on day 30 after implantation, and a subsequent increase in volume on day 40 after implantation after IR (Fig. S1e and f†). In addition, we found that radiation treatment substantially prolonged the survival of glioma-bearing mice by 38.5% (Fig. S1g†). Immunofluorescence staining revealed a dramatically increased proposition of Fn14^{+} glioma in residual tumors after irradiation (up to 40.0%) (Fig. 1f and g). Furthermore, over 51.4% of tumor cells were Fn14^{+} cells within the residual foci in mice treated with irradiation. Overall, these data indicated that Fn14^{+} GBM cells were the predominant population in residual sites after radiotherapy.

To rule out the possibility that radiation may upregulate Fn14 gene expression in GBM cells, we detected the Fn14 expression at different time points after receiving irradiation (Fig. S1h†). However, the results suggested that irradiation had no considerable effect on the expression of Fn14 in U251 cells.

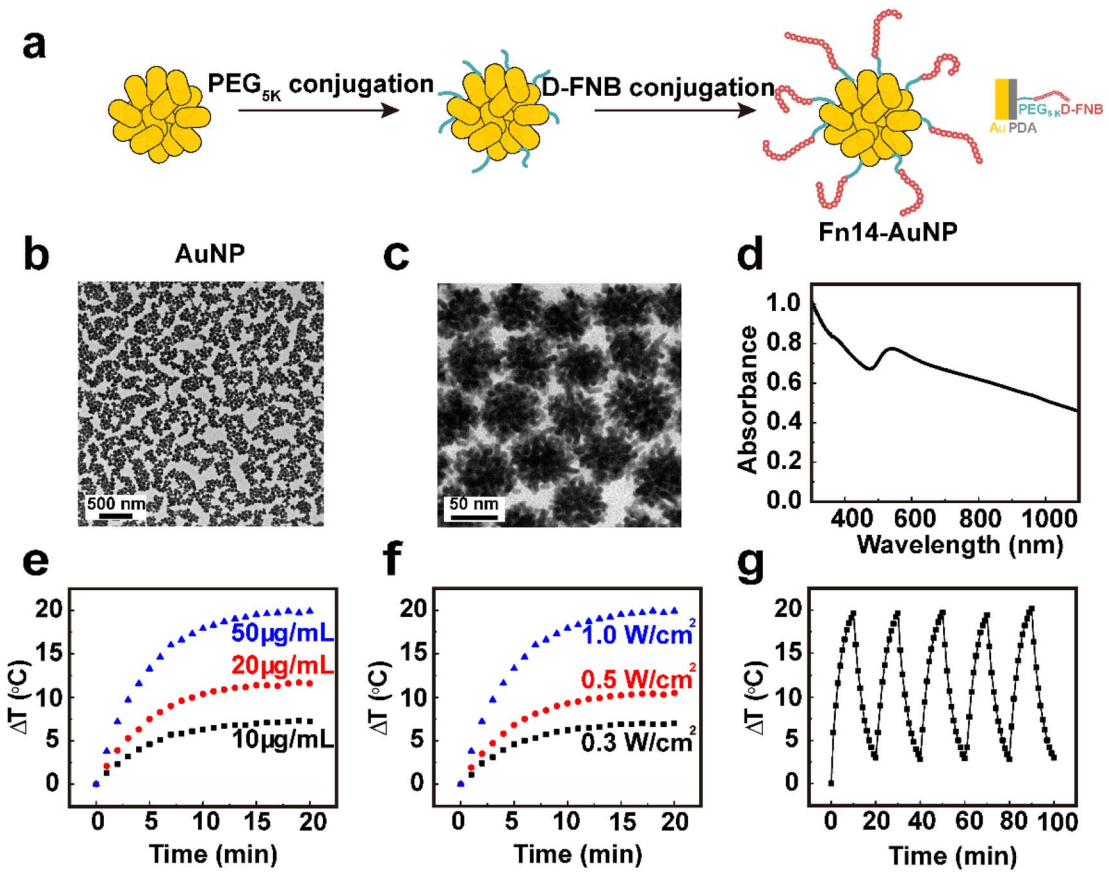

Fig. 2 Characterization of Fn14-AuNPs. (a) Illustrative diagram for the synthesis of Fn14-AuNPs. (b) and (c) TEM images of Fn14-AuNPs (scale bar: 500 nm and 50 nm). (d) Absorption spectra of Fn14-AuNPs (50 μg ml^{-1}). (e) Laser irradiation at 1064 nm and 1.0 W cm^{-2} increased the temperature of Fn14-AuNPs solutions at concentrations of 10, 20, and 50 μg ml^{-1}. (f) Laser irradiation using different power intensities (0.3, 0.5 and 1.0 W cm^{-2}) caused temperature increases in the Fn14-AuNPs solution (50 μg ml^{-1}). (g) Heating–cooling curve of Fn14-AuNPs solution (50 μg ml^{-1}) under repeated laser exposure (1.0 W cm^{-2}).

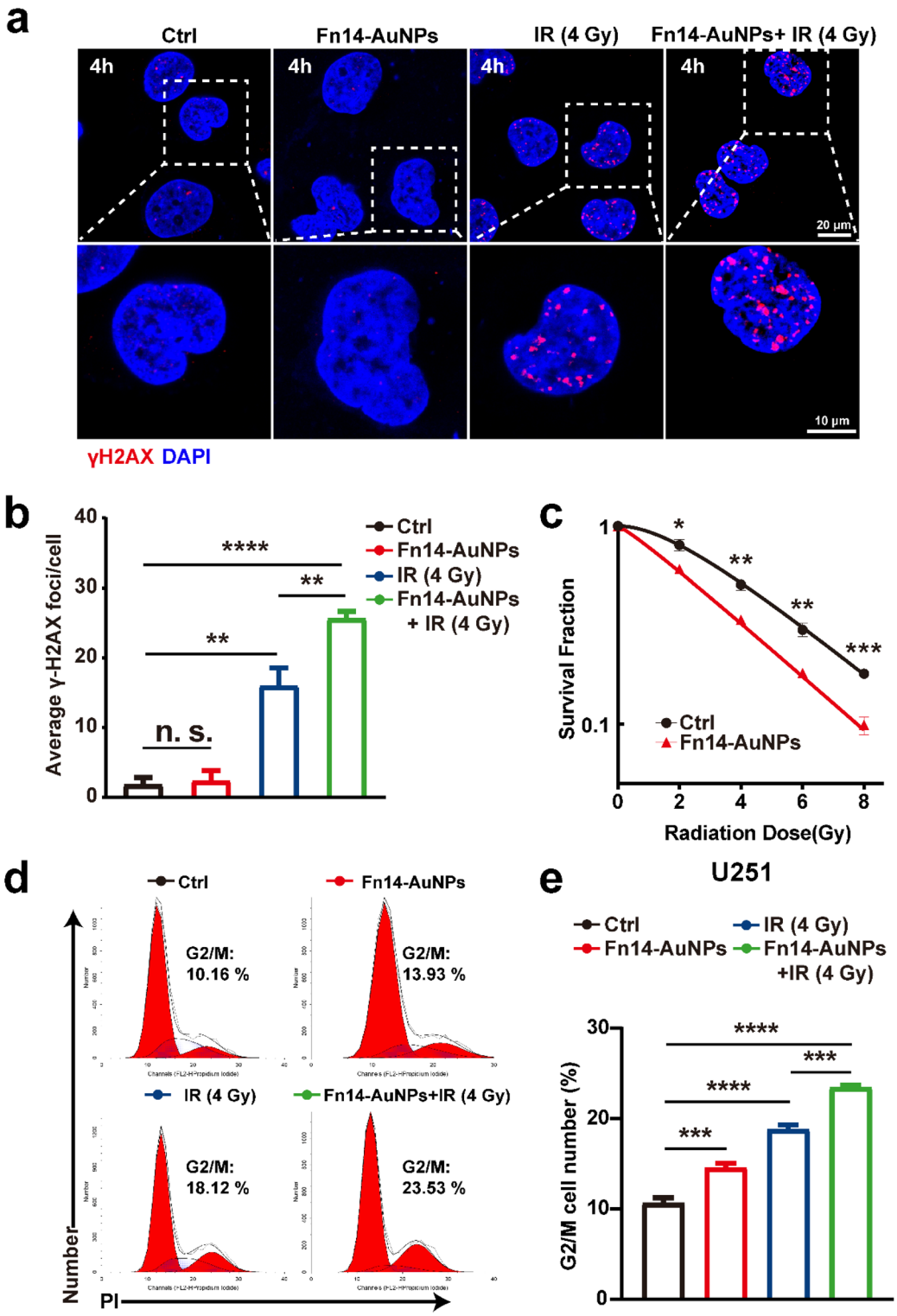

Fig. 3 Fn14-AuNPs enhanced the radiosensitivity of Fn14^{OE} glioma cells *in vitro*. (a) Fluorescence staining images and (b) quantification of γH2AX foci in Fn14^{OE} U251 cells at 4 h after different treatments (Ctrl, Fn14-AuNPs, IR (4 Gy), and Fn14-AuNPs + IR (4 Gy); scale bar: 20 μm (upper row) and 10 μm (lower row). (c) Clonogenic survival assay of Fn14^{OE} U251 cells treated with Fn14-AuNPs. Fn14^{OE} U251 cells were exposed to physical radiation doses of 0 Gy, 2 Gy, 4 Gy, 6 Gy, and 8 Gy, and the cell colonies with ≥50 cells were statistically analyzed after 2 weeks. (d) Representative flow cytometry histogram of cell-cycle analysis in Fn14^{OE} U251 cells after 24 h of indicated treatments: Ctrl, Fn14-AuNPs, IR (4 Gy), and Fn14-AuNPs + IR (4 Gy). (e) Quantification of the cell distribution in the G_2/M phase of the cell cycle. Data are presented as mean ± SD, with $n = 3$ per group. Statistical significance is indicated as follows: n. s. (no significance), *$p < 0.05$, **$p < 0.01$, ***$p < 0.001$, ****$p < 0.0001$.

Thus, one alternative explanation is that $Fn14^{+}$ cells enriched in GBM after irradiation are intrinsically resistant to radiotherapy.

The nanoplatform containing an AuNP core and a mesoporous polydopamine (mPDA) shell has been established in our previous work, showing efficient photothermal conversion and peptide cargo loading.[22,39,40] Herein, we designed peptide-functionalized AuNPs to target Fn14 positive subpopulation and enhance cellular uptake. As described previously, AuNPs were synthesized using the one-pot seedless and surfactant-free method.[41] The D-enantiomeric peptide ligand of Fn14 (D-FNB, sequenced as $^{D}C^{D}H^{D}P^{D}P^{D}R^{D}E^{D}V^{D}D^{D}V^{D}E^{D}L^{D}Y^{D}S^{D}T^{D}V^{D}F^{D}G^{D}H$) was artificially synthesized and mixed with the AuNPs solution, forming Fn14-AuNPs nanoparticles (Fig. 2a). During the manufacturing process, H_2N-PEG-NH_2 (MW = 5 kDa) was added to improve the colloidal stability of AuNPs in blood circulation and facilitate the conjugation of D-FNB onto AuNPs. In addition, previous studies showed that PEG surface modification reduced protein corona formation and RES clearance, resulting in superior pharmacokinetic and bioavailability properties.[42,43]

Transmission electron microscopy (TEM) images demonstrated that the structure of Fn14-AuNPs was a hyperbranched and compact framework (Fig. 2b and c). The plasmonic coupling between adjacent branches endowed Fn14-AuNPs absorption across UV-vis-NIR spectra (Fig. 2d). Furthermore, the high absorption and scattering ratio of Fn14-AuNPs, attributed to their hyperbranched structure, led to superior photothermal conversion efficiency. The temperature variations of Fn14-AuNPs solutions were recorded at several concentrations (10, 20 and 50 μg ml^{-1}) with the maximum permission exposure (MPE) of NIR-II laser (1.0 W cm^{-2}, 1064 nm). Within 10 min, the temperature of Fn14-AuNPs (50 μg ml^{-1}) increased rapidly by 17.5 °C (Fig. 2e). It was also exhibited in Fig. 2f that the temperature of Fn14-AuNPs solution (50 μg ml^{-1}) ascended with irradiation time when received to different power intensities (0.33, 0.5 and 1.0 W cm^{-2}) of NIR-II laser. To test the photothermal stability of Fn14-AuNPs, this irradiation was applied to the Fn14-AuNPs solution (50 μg ml^{-1}) for about 10 min (1.0 W cm^{-2}) and repeated for five cycles (Fig. 2g). The peak temperature of Fn14-AuNPs solution in every heating–cooling cycle was retained identically, strongly indicating its photothermal and structural stability.

3.2 Fn14-AuNPs enhanced the radiosensitivity of $Fn14^{OE}$ glioma cells *in vitro*

The therapeutic efficacy of Fn14-AuNPs will be significantly affected by the tumor targeting. Thus, we first evaluated the ability of Fn14-AuNPs to target $Fn14^{OE}$ glioma cells. $Fn14^{OE}$ U251 cells were co-cultured with Fn14-AuNPs (150 μg ml^{-1}) for 2 h. TEM imaging revealed that Fn14-AuNPs exhibited enhanced cell membrane adherence and internalization compared to the AuNPs group, implying a remarkable capacity for targeting Fn14-AuNPs *in vitro* (Fig. S2a†). The introduction of nanoparticles with high atomic numbers into tumors has been developed for enhanced radiosensitivity due to their enzyme-like catalytic activity, production of ROS, disruption of radiation-induced DNA damage repair, induction of G_2/M cell cycle arrest and inhibition of hypoxia.[44,45] To this point, we evaluated the potential radiosensitizing effect of Fn14-AuNPs on $Fn14^{OE}$ U251 cells. As shown in Fig. 3a and b, an increased γ-H2AX foci formation upon IR was noted in $Fn14^{OE}$ cells pretreated with Fn14-AuNPs when compared to the other groups, indicating an enhanced radiosensitivity associated with Fn14-AuNPs. In line with these results, the colony formation assay also exhibited that Fn14-AuNPs nanoparticles could suppress the $Fn14^{OE}$ U251 cell proliferation (Fig. 3c). Previous studies have shown that gold nanoparticles can promote radiation-induced G_2/M arrest, thereby enhancing radiosensitivity.[46,47] Therefore, we subsequently assessed the cell cycle distribution with flow cytometry. Compared to Ctrl groups, the G_2/M arrest was dramatically induced by pretreatment with Fn14-AuNPs (23.5% of Fn14-AuNPs *vs.* 18.1% of Ctrl, $*p < 0.05$) (Fig. 3d and e). Taken together, these results verified the potential of FN14-AuNPs nanoparticles to radiosensitize $Fn14^{OE}$ U251 cells *in vitro*.

3.3 Fn14-AuNPs-mediated mPTT further increased the radiosensitivity of $Fn14^{OE}$ glioma cells *in vitro*

Mild photothermal therapy (mPTT), which converts light energy to mild heat energy, is an emerging strategy that renders cancer cells more vulnerable to treatment modalities including radiotherapy, chemotherapy and immunotherapy.[48–50] Lower hyperthermia (<45 °C) can avoid collateral damage to healthy tissues and tumor metastasis resulting from excessive hyperthermia during cancer therapy. Notably, recent research suggested that mPTT can disrupt DNA damage repair pathways by affecting several critical repair mechanisms, including translesion DNA synthesis, nucleotide excision repair,[51] base excision repair,[52] mismatch repair,[53] homologous recombination and non-homologous end joining.[54] mPTT is expected to enhance the efficacy of genotoxic therapies such as radiotherapy by preventing the repair of radiation-induced damage.[50] Thus, to investigate whether Fn14-mediated mPTT can augment the radiosensitivity of $Fn14^{OE}$ U251 cells, we treated $Fn14^{OE}$ U251 cells with Fn14-AuNPs for 24 h, followed by laser irradiation. An infrared thermal camera was employed to monitor the photothermal temperature in real time. The colony formation assay confirmed that pretreatment with Fn14-AuNPs-based mPTT suppressed cell proliferation (Fig. 4a and b). Similarly, the cell cycle distribution in Fig. 5c and d demonstrated that pretreatment with mPTT significantly induced G_2/M arrest and inhibited cell proliferation caused by irradiation (29.9% in the thermoradiotherapy group *vs.* 17.6% in the radiotherapy-only group, $*p < 0.05$). The cell viability was 95% in the group treated with mPTT (42.5 °C), whereas the viability of the cells treated with high-temperature PTT (48 °C) decreased to 20.0% (Fig. S2b†). Live/dead co-staining (live cells with AM; dead cells with PI) also demonstrated a comparable pattern (Fig. S2c†). These data indicated that mPTT alone cannot directly kill tumor cells or cause any DNA DSBs. Notably, we observed a significant outcome in the Fn14-AuNPs + mPTT + IR group, where cells were irradiated following hyperthermia (approximately an

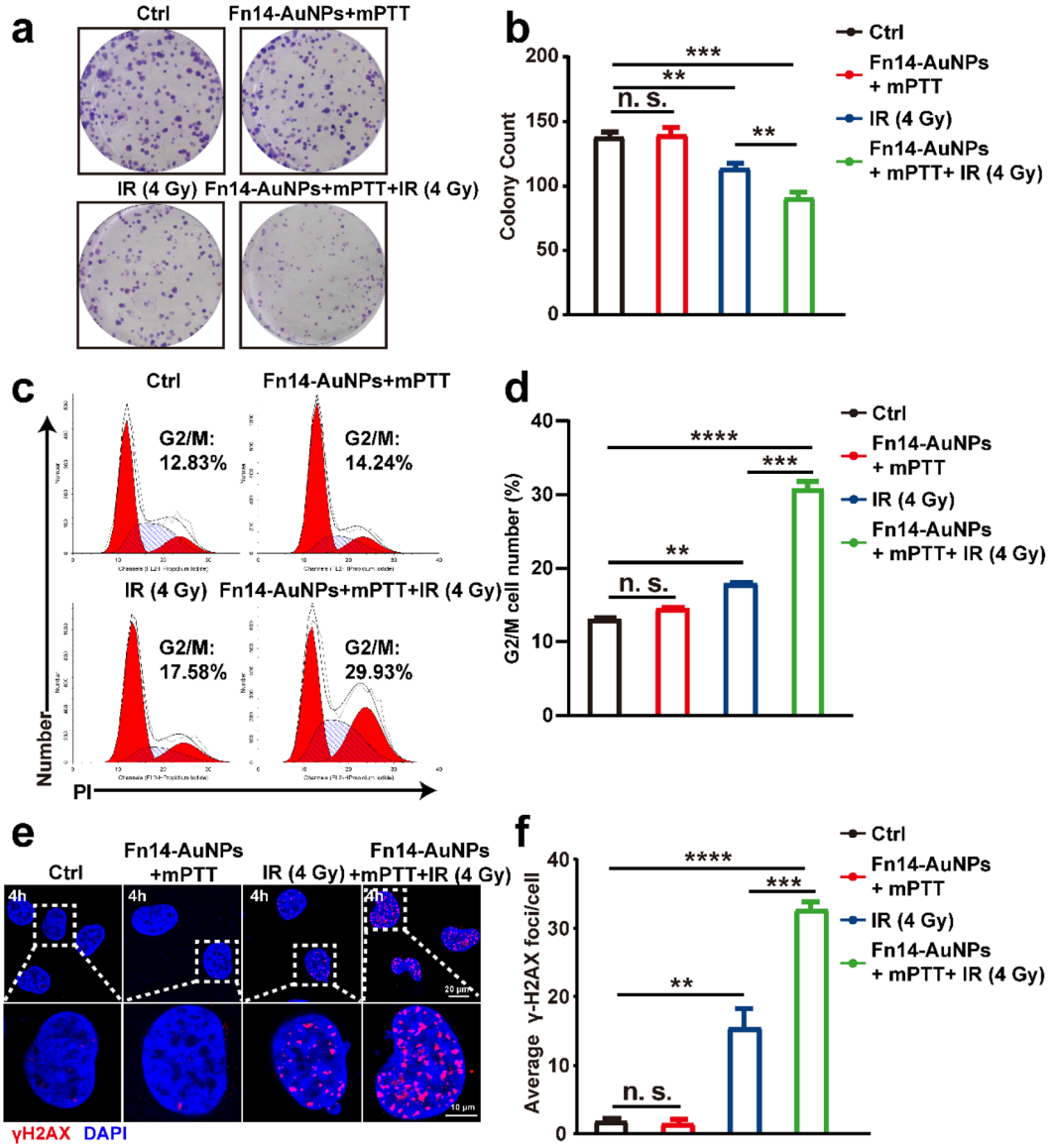

Fig. 4 Fn14-AuNPs-mediated mPTT further increased the radiosensitivity of $Fn14^{OE}$ glioma cells *in vitro*. (a) and (b) representative images of colony formation and colony count of $Fn14^{OE}$ U251 cells in Ctrl, Fn14-AuNPs + mPTT, IR (4 Gy), Fn14-AuNPs + mPTT + IR (4 Gy) groups.(c) and (d) Cell cycle plot and its quantification displaying the percentage of G_2/M phase in $Fn14^{OE}$ U251 cells after 24 h of indicated treatments (Ctrl, Fn14-AuNPs + mPTT, IR (4 Gy), Fn14-AuNPs + mPTT + IR (4 Gy)) (e) and (f) fluorescence staining images and quantification of γ-H2AX foci in $Fn14^{OE}$ U251 cells at 4 h after different treatments: Ctrl, Fn14-AuNPs + mPTT, IR (4 Gy), Fn14-AuNPs + mPTT + IR (4 Gy) groups scale bar: 20 μm (upper row) and 10 μm (lower row). Data are presented as mean ± SD, with $n = 3$ per group. Statistical significance is indicated as follows: n. s. (no significance), $^{**}p < 0.01$, $^{***}p < 0.001$, $^{****}p < 0.0001$.

interval of 10 minutes between the two treatments). And that was a remarkable increase in the level of γ-H2AX in the thermoradiotherapy group (Fig. 4e and f). These results implied that Fn14-AuNPs-based mPTT could efficiently promote radiation-induced DNA DSBs and prevent DNA damage repair, rather than directly eliminate tumor cells.

A study has revealed that applying hyperthermia before radiotherapy can effectively suppress the activation of AKT signaling in GBM cells.[15] Moreover, another research has reported that the abnormal activation of the AKT signaling was strongly associated with radioresistance in GBM.[38] Based on these, we speculated that mPTT sensitized GBM cells to radiation by suppressing the abnormal activation of the AKT signaling pathway. Consistent with our hypothesis, the Fn14-AuNPs + mPTT + IR group exhibited reduced expression levels of p-AKT and p-DNA-PKcs compared to other IR-treated groups (Fig. S2d†). This indicated that Fn14-AuNPs-mediated mPTT could radiosensitize $Fn14^{OE}$ U251 cells by inhibiting the DNA damage checkpoint response.

3.4 The tumor targeting and BBB-crossing capabilities of Fn14-AuNPs *in vitro* and *in vivo*

The BBB, a selective barrier formed by endothelial cells, astrocytes, pericytes, and tight junctions also restricts the entry of drugs into the brain parenchyma, eventually leading to the

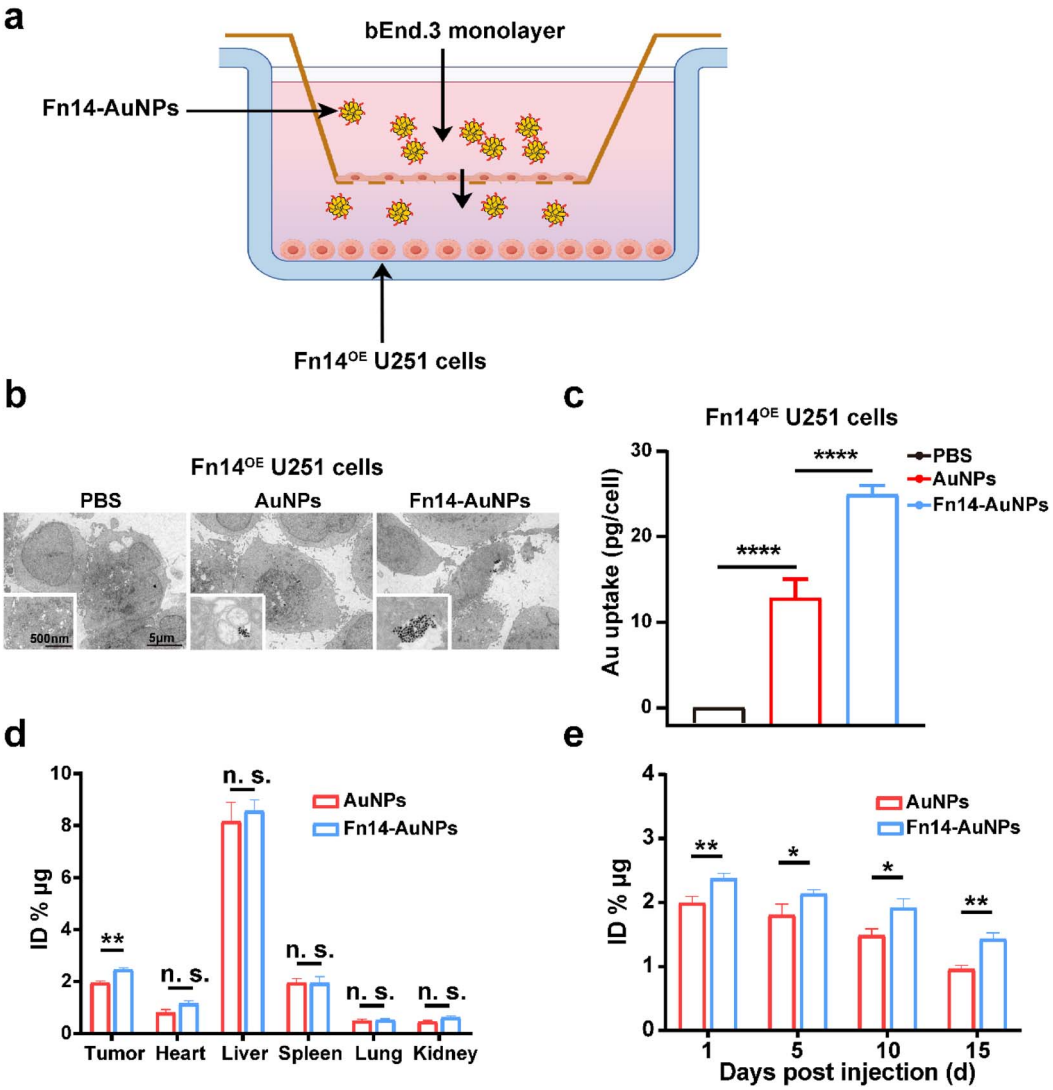

Fig. 5 The BBB-crossing ability of Fn14-AuNPs *in vitro* and *in vivo*. (a) Schematic representation of the *in vitro* BBB model. (b) Representative TEM images of the uptake of nanoparticles in Fn14^{OE} U251 cells across different groups (PBS, AuNPs, Fn14-AuNPs, AuNPs + NIR, Fn14-AuNPs + NIR). Scale bar: 5 μm and 500 nm. (c) The intracellular gold accumulation in Fn14-Fn14^{OE} glioma cells after 6 h of different treatments: PBS (Ctrl), AuNPs, Fn14-AuNPs, AuNPs with NIR and Fn14-AuNPs with NIR. (d) The ICP-MS analysis of Fn14-AuNPs accumulation in major organs and tumors from AuNPs and Fn14-AuNPs injected orthotopic tumor-bearing mice *in vivo*. (e) Retention ability of AuNPs and Fn14-AuNPs in tumor tissues of Fn14^{OE} U251 cells orthotopic tumor-bearing murine model after tail vein injection quantified by ICP-MS at different time points. Data are presented as mean ± SD, with $n = 3$ per group. Statistical significance is indicated as follows: n. s. (no significance), *$p < 0.05$, **$p < 0.01$, ****$p < 0.0001$.

failure of cancer treatments.[55,56] To assess the BBB penetration capability of Fn14-AuNPs, we constructed a transwell assay consisting of bEnd.3 cells to mimic the BBB as illustrated in Fig. 5a. The high TEER of approximately 150 Ω cm^2 confirmed the integrity of the BBB model for studying Fn14-AuNPs transport[57–59] (Fig. S2e†). In this model, the TEM imaging displayed that Fn14-AuNPs exhibited enhanced cell membrane adherence and internalization compared to the AuNPs and PBS groups in Fn14^{OE} glioma cells (Fig. 5b). Moreover, the ICP-MS analysis demonstrated a higher upake of Fn14-AuNPs by Fn14^{OE} glioma cells compared to the AuNPs and PBS groups (Fig. 5c). These results indicated that Fn14-AuNPs had a superior BBB penetration ability *in vitro*. Previous studies have shown that AuNPs can cross BBB *via* passive diffusion in Transwell and Microfluidic models *in vitro*, owing to their small size of less than 50 nm.[24,60–62] Therefore, the excellent BBB penetration capability of Fn14-AuNPs may be attributed to their small particle size, which makes it easier for them to traverse the gaps between endothelial cells.

To further explore the tumor targeting and BBB-crossing capabilities *in vivo*, the biodistribution of AuNPs and Fn14-AuNPs was investigated by ICP-MS 24 h after injection of Fn14-AuNPs (150 μg ml^{-1}, 100 μl per mouse) in Fn14^{OE} U251 orthotopic tumor-bearing mice. The accumulation of elemental Au in the brain tumor 24 h after Fn14-AuPB treatment (Fig. 5d) indicated that Fn14-AuNPs also had an excellent BBB

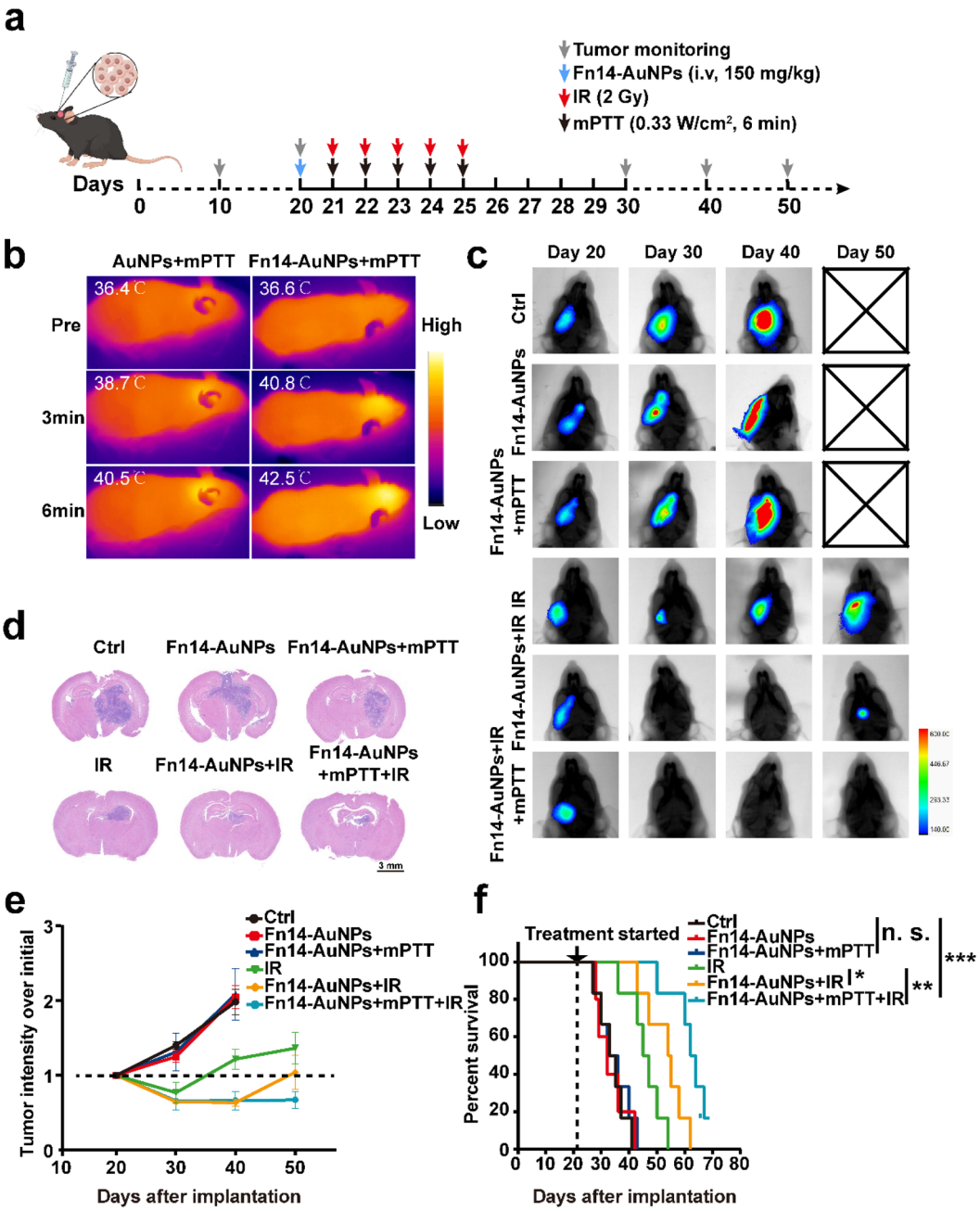

Fig. 6 *In vivo* Fn14-AuNPs-mediated mPTT suppressed GBM progression (a) a diagram illustrating the experimental design *in vivo*. (b) Representative images of the temperature elevation during photothermal therapy ($n = 6$ per group). (c) Representative bioluminescence assay images of various treatment groups ($n = 4$ per group). (d) H&E images of mice brain tissues with tumors from various groups were acquired 10 days after tumor implantation (scale bar: 3 mm). (e) The quantitative signal intensity of bioluminescence assay. (f) Kaplan–Meier survival curves for mice intracranially injected with Fn14OE U251 cells and subjected to various treatments ($n = 6$ per group). Statistical significance was assessed using an unpaired Student's *t*-test, with results presented as mean ± SD (n. s., no significance, $^{**}p < 0.01$, $^{***}p < 0.001$).

penetration ability *in vivo*. In addition, to evaluate the retention time of AuNPs and Fn14-AuNPs, tumor tissues were harvested from orthotopic $Fn14^{OE}$ U251 tumor-bearing mice at 1, 5, 10, and 15 days following AuNPs and Fn14-AuNPs injection. To evaluate nanoparticle accumulation in tissues, the elemental Au concentration was measured through ICP-MS analysis. As shown in Fig. 5e, the retention time of Fn14-AuNPs or AuNPs in tumors exceeded 15 days, confirming their long-term aggregation at the targeted location following a single dose of Fn14-AuNPs or AuNPs. Overall, these results indicated that Fn14-AuNPs had excellent BBB penetration and tumor-targeting abilities both *in vitro* and *in vivo*.

3.5 Biosafety assessment of Fn14-AuNPs

The biosafety of Fn14-AuNPs was assessed both *in vitro* and *in vivo* to ascertain their suitability for anticancer therapies. The cytotoxicity of Fn14-AuNPs was evaluated in human GBM cells

(Fn14^{OE} U251) and murine microglia cells (BV2) after incubation with Fn14-AuNPs for 24 h by CCK-8 assay. As shown in Fig. S3a and b,† cell viability was maintained at 94% in both Fn14^{OE} U251 and BV2 cells, suggesting that the Fn14-AuNPs had no noticeable cytotoxicity *in vitro*. To assess the *in vivo* toxicity of Fn14-AuNPs, mice were divided into PBS group (100 μl per mouse), AuNPs group (100 μl per mouse, 150 μg ml^{-1}), or Fn14-AuNPs group (100 μl per mouse, 150 μg ml^{-1}) (n = 3/group). The weight of mice was measured every two days within 2 weeks. No body weight loss was observed in any of the groups (Fig. S3c†). We further investigated the biocompatibility of AuNPs or Fn14-AuNPs *via* the H&E staining and blood biochemistry on healthy tissues. Two weeks after the injection, blood chemistry and complete blood count tests were performed. Quantitative analysis of blood tests revealed no notable differences between the Ctrl (PBS) and nanoparticle-treated groups (Fig. S3d and e†). These findings verified that repeated nanoparticle treatments had no harm to the liver, kidney or hematological parameters. Meanwhile, samples from major organs (heart, liver, kidney, spleen and lung) were collected two weeks after injection and subjected to H&E staining. Tissue histopathology indicated that there was no inflammation, ischemia, necrosis, or other histological or architectural irregularities in these organs, indicating that they were not affected by AuNPs or Fn14-AuNPs and maintained physiological condition (Fig. S3f†). These results confirmed the nontoxicity of AuNPs or Fn14-AuNPs in mice.

3.6 *In vivo* Fn14-AuNPs-mediated mPTT suppressed GBM progression

To assess the synergistic efficiency of radiotherapy combined with Fn14-AuNPs + mPTT, orthotopic Fn14^{OE} U251 tumor-bearing mice were randomly allocated into six groups: (i) Ctrl; (ii) Fn14-AuNPs (150 μg ml^{-1}, 100 μl per mouse); (iii) Fn14-AuNPs + mPTT (0.33 W cm^{-2}, 6 min); (iv) IR (10 Gy in total, 2 Gy per day for 5 days); (v) Fn14-AuNPs + IR; (vi) Fn14-AuNPs + mPTT plus IR. The treatment strategy was represented in Fig. 6a. Mice received a dose of Fn14-AuNPs (intravenous injection, *i.v*) followed by exposure to 1064 nm laser irradiation (0.33 W cm^{-2}, 6 min). During the treatment, the local temperature in tumor-bearing mice administered AuNPs or Fn14-AuNPs was monitored. Within 6 minutes, the temperature in the tumor region injected with Fn14-AuNPs increased quickly from 36.6 °C to 42.5 °C (Fig. 6b). The treatment temperature was sustained at about 42.5 °C. Radiotherapy commenced within 10 minutes following the completion of mPTT. The therapeutic effect was assessed by the tumor growth (bioluminescence signals from Fn14^{OE} U251 cells) and overall survival rates. Tumor progression was considerably inhibited after treatment with IR, Fn14-AuNPs + IR and Fn14-AuNPs + mPTT + IR, as evidenced by lower tumorous luciferase intensity (Fig. 6c and 5e) and H&E images (Fig. 6d). Compared to the other groups, the Fn14-AuNPs + mPTT + IR group achieved the most prominent antitumor effects with no obvious neurological symptoms observed at 50 days after tumor implantation. Consequently, the group of mice treated with Fn14-AuNPs + mPTT + IR exhibited a dramatically prolonged lifespan. Fn14-AuNPs + mPTT + IR extended the median survival of Fn14^{OE} U251-bearing mice to 62 days, a 1.8-fold increase in comparison to the Ctrl group. As shown by Fig. 6f, the other groups without IR including Ctrl, Fn14-AuNPs, and Fn14-AuNPs + mPTT illustrated a limited lifespan, with a median survival of only 34.6 days. IR and Fn14-AuNPs + IR treatment moderately improved survival to 45.8 days, and 53.2 days respectively. In summary, these observations implied that Fn14-AuNPs-mediated mPTT boosted the antitumor therapeutic effect of radiotherapy.

4. Conclusions

In summary, our study revealed that high Fn14 expression correlated with poor clinical outcomes in GBM patients. Furthermore, Fn14^{+} glioma cells predominated in the residual sites of GBM following radiotherapy, potentially due to the preferential activation of DNA damage checkpoint response. Based on these findings, we developed a photonic and targeted nanoparticle designated as Fn14-AuNPs. The AuNPs core provided the foundation for light-to-heat conversion, while the D-FNB served as the targeting ligand, facilitating the attachment of Fn14-AuNPs to Fn14-expressing glioma cells. Fn14-AuNPs also had the excellent BBB-crossing capabilities and the advantage of sustained retention at targeted sites, along with their established biocompatibility and biosafety. The properties of the gold nanoparticles made Fn14-AuNPs ideal candidates as radiosensitizers. Notably, the therapeutic combination of IR + Fn14-AuNPs and mPTT further boosted the radiosensitivity of Fn14-positive cells because of the mPTT-activated DNA damage checkpoint response. *In vivo*, utilization of IR + Fn14-AuNPs + mPTT also remarkably suppressed tumor growth. Overall, given the significant role of Fn14 in the radiosensitivity of glioma cells, the combined utilization of IR and Fn14-AuNPs-mediated mPTT is anticipated to be a novel therapeutic approach to enhance radiosensitivity and improve the efficiency of radiotherapy in GBM.

Ethical statement

Animal experiments adhered to the ethical guidelines of the Animal Ethics Committee at Tongji Medical College, Huazhong University of Science and Technology (IACUC Number 3066).

Consent for publication

The authors agree to publication.

Data availability

All data regarding this manuscript are already shown in the graphs of the main paper.

Author contributions

The authors confirmed their contribution to the paper as follows: Wei Fu, Jinghua Ren designed the experiments. Qing

Liang and Wei Fu performed experiments and collected data. Qing Liang, Wei Fu and Shiqiong Lei, Ruiqi Li, Xin Zheng and Lian Chen contributed to data analysis. Qing Liang, Wei Fu, Yuxi Ma and Jinghua Ren wrote the manuscript. Xiaofang Dai, Hongwei Duan, Wenshan He and Jinghua Ren supervised, directed, and managed the study.

Conflicts of interest

There are no competing interests.

Acknowledgements

This work was supported by Natural Science Foundation of Hubei Province (No. 2020CFB786), National Natural Science Foundation of China (No. 82072944, 81874084, 82072800 and 82103385), and Science, Technology and Innovation Commission of Shenzhen Municipality (JCYJ20210324141802006).

References

1 L. Rong, N. Li and Z. Zhang, *J. Exp. Clin. Cancer Res.*, 2022, **41**, 142.
2 C. W. Brennan, R. G. Verhaak, A. McKenna, B. Campos, H. Noushmehr, S. R. Salama, S. Zheng, D. Chakravarty, J. Z. Sanborn, S. H. Berman, R. Beroukhim, B. Bernard, C. J. Wu, G. Genovese, I. Shmulevich, J. Barnholtz-Sloan, L. Zou, R. Vegesna, S. A. Shukla, G. Ciriello, W. K. Yung, W. Zhang, C. Sougnez, T. Mikkelsen, K. Aldape, D. D. Bigner, E. G. Van Meir, M. Prados, A. Sloan, K. L. Black, J. Eschbacher, G. Finocchiaro, W. Friedman, D. W. Andrews, A. Guha, M. Iacocca, B. P. O'Neill, G. Foltz, J. Myers, D. J. Weisenberger, R. Penny, R. Kucherlapati, C. M. Perou, D. N. Hayes, R. Gibbs, M. Marra, G. B. Mills, E. Lander, P. Spellman, R. Wilson, C. Sander, J. Weinstein, M. Meyerson, S. Gabriel, P. W. Laird, D. Haussler, G. Getz and L. Chin, *Cell*, 2013, **155**, 462–477.
3 V. M. Ravi, P. Will, J. Kueckelhaus, N. Sun, K. Joseph, H. Salié, L. Vollmer, U. Kuliesiute, J. von Ehr, J. K. Benotmane, N. Neidert, M. Follo, F. Scherer, J. M. Goeldner, S. P. Behringer, P. Franco, M. Khiat, J. Zhang, U. G. Hofmann, C. Fung, F. L. Ricklefs, K. Lamszus, M. Boerries, M. Ku, J. Beck, R. Sankowski, M. Schwabenland, M. Prinz, U. Schüller, S. Killmer, B. Bengsch, A. K. Walch, D. Delev, O. Schnell and D. H. Heiland, *Cancer Cell*, 2022, **40**, 639–655.e613.
4 K. Yang, Z. Wu, H. Zhang, N. Zhang, W. Wu, Z. Wang, Z. Dai, X. Zhang, L. Zhang, Y. Peng, W. Ye, W. Zeng, Z. Liu and Q. Cheng, *Mol. Cancer*, 2022, **21**, 39.
5 I. Dagogo-Jack and A. T. Shaw, *Nat. Rev. Clin. Oncol.*, 2018, **15**, 81–94.
6 T. Kondo, *Semin. Cancer Biol.*, 2022, **82**, 176–183.
7 E. Verdugo, I. Puerto and M. Medina, *Cancer Commun.*, 2022, **42**, 1083–1111.
8 D. Nehama, A. S. Woodell, S. M. Maingi, S. D. Hingtgen and G. Dotti, *Neuro Oncol.*, 2023, **25**, 1551–1562.
9 A. Marusyk, M. Janiszewska and K. Polyak, *Cancer Cell*, 2020, **37**, 471–484.
10 M. J. van den Bent, M. Geurts, P. J. French, M. Smits, D. Capper, J. E. C. Bromberg and S. M. Chang, *Lancet*, 2023, **402**, 1564–1579.
11 Y. Wu, Y. Song, R. Wang and T. Wang, *Mol. Cancer*, 2023, **22**, 96.
12 D. Antoni, L. Feuvret, J. Biau, C. Robert, J. J. Mazeron and G. Noël, *Cancer Radiother.*, 2022, **26**, 116–128.
13 L. Barthel, M. Hadamitzky, P. Dammann, M. Schedlowski, U. Sure, B. K. Thakur and S. Hetze, *Cancer Metastasis Rev.*, 2022, **41**, 53–75.
14 Y. A. Yabo, S. P. Niclou and A. Golebiewska, *Neuro Oncol.*, 2022, **24**, 669–682.
15 J. Man, J. D. Shoemake, T. Ma, A. E. Rizzo, A. R. Godley, Q. Wu, A. M. Mohammadi, S. Bao, J. N. Rich and J. S. Yu, *Cancer Res.*, 2015, **75**, 1760–1769.
16 A. Ou, W. K. A. Yung and N. Majd, *Int. J. Mol. Sci.*, 2020, **22**, 351.
17 L. C. Burkly, *Semin. Immunol.*, 2014, **26**, 229–236.
18 J. G. Perez, N. L. Tran, M. G. Rosenblum, C. S. Schneider, N. P. Connolly, A. J. Kim, G. F. Woodworth and J. A. Winkles, *Oncogene*, 2016, **35**, 2145–2155.
19 H. Wajant, *Br. J. Pharmacol.*, 2013, **170**, 748–764.
20 C. Mochizuki, J. Nakamura and M. Nakamura, *ACS Omega*, 2023, **8**, 9569–9582.
21 J. Atkinson, J. Chopin, E. Bezak, H. Le and I. Kempson, *Chemphyschem*, 2024, **26**, e202400764.
22 Q. Liang, J. Chen, S. Hou, D. Li, Y. Zhu, R. Li, L. Chen, J. Li, W. Fu, S. Lei, B. Zhang, X. Zheng, T. Zhang, H. Duan, W. He and J. Ren, *Biomaterials*, 2023, **300**, 122206.
23 S. Zha, H. Liu, H. Li, H. Li, K. L. Wong and A. H. All, *ACS Nano*, 2024, **18**, 1820–1845.
24 Y. Fan, C. Xu, N. Deng, Z. Gao, Z. Jiang, X. Li, Y. Zhou, H. Pei, L. Li and B. Tang, *Lab Chip*, 2023, **23**, 1935–1944.
25 S. Chen, J. Liu, M. Yang, W. Lai, L. Ye, J. Chen, X. Hou, H. Ding, W. Zhang, Y. Wu, X. Liu, S. Huang, X. Yu and D. Xiao, *PLoS One*, 2015, **10**, e0143802.
26 S. Zhang, Y. Hu, Z. Wu, X. Zhou, T. Wu, P. Li, Q. Lian, S. Xu, J. Gu, L. Chen, G. Wu, T. Zhang, J. Tang and J. Xue, *Int. J. Radiat. Oncol. Biol. Phys.*, 2023, **115**, 1244–1256.
27 J. H. Pedder, A. M. Sonabend, M. D. Cearns, B. D. Michael, R. Zakaria, A. B. Heimberger, M. D. Jenkinson and D. Dickens, *Lancet Neurol.*, 2025, **24**, 246–260.
28 S. Sato, Y. J. Tang, Q. Wei, M. Hirata, A. Weng, I. Han, A. Okawa, S. Takeda, H. Whetstone, P. Nadesan, D. G. Kirsch, J. S. Wunder and B. A. Alman, *Cell Rep.*, 2016, **16**, 917–927.
29 S. Liu, F. Yin, W. Fan, S. Wang, X. R. Guo, J. N. Zhang, Z. M. Tian and M. Fan, *J. Exp. Clin. Cancer Res.*, 2012, **31**, 52.
30 U. Ahmadov, D. Picard, J. Bartl, M. Silginer, M. Trajkovic-Arsic, N. Qin, L. Blümel, M. Wolter, J. K. M. Lim, D. Pauck, A. M. Winkelkotte, M. Melcher, M. Langini, V. Marquardt, F. Sander, A. Stefanski, S. Steltgens, C. Hassiepen, A. Kaufhold, F. D. Meyer, A. Seibt, L. Kleinesudeik, A. Hain, C. Münk, C. B. Knobbe-Thomsen, A. Schramm, U. Fischer, G. Leprivier, K. Stühler, S. Fulda, J. T. Siveke,

F. Distelmaier, A. Borkhardt, M. Weller, P. Roth, G. Reifenberger and M. Remke, *Cell Death Dis.*, 2021, **12**, 885.
31 R. Li, L. Chen, Q. Ji, Q. Liang, Y. Zhu, W. Fu, T. Chen, H. Duan, W. He, Z. Xu, X. Dai and J. Ren, *Adv. Funct. Mater.*, 2023, **33**, 2213292.
32 S. P. Fortin, M. J. Ennis, B. A. Savitch, D. Carpentieri, W. S. McDonough, J. A. Winkles, J. C. Loftus, C. Kingsley, G. Hostetter and N. L. Tran, *Mol. Cancer Res.*, 2009, **7**, 1871–1881.
33 C. S. Schneider, J. G. Perez, E. Cheng, C. Zhang, P. Mastorakos, J. Hanes, J. A. Winkles, G. F. Woodworth and A. J. Kim, *Biomaterials*, 2015, **42**, 42–51.
34 D. S. Hersh, B. G. Harder, A. Roos, S. Peng, J. E. Heath, T. Legesse, A. J. Kim, G. F. Woodworth, N. L. Tran and J. A. Winkles, *Neuro Oncol.*, 2018, **20**, 1321–1330.
35 J. A. Winkles, N. L. Tran and M. E. Berens, *Cancer Lett.*, 2006, **235**, 11–17.
36 M. Gerić, G. Gajski and V. Garaj-Vrhovac, *Ecotoxicol. Environ. Saf.*, 2014, **105**, 13–21.
37 M. Martini, M. C. De Santis, L. Braccini, F. Gulluni and E. Hirsch, *Ann. Med.*, 2014, **46**, 372–383.
38 M. Toulany, K. J. Lee, K. R. Fattah, Y. F. Lin, B. Fehrenbacher, M. Schaller, B. P. Chen, D. J. Chen and H. P. Rodemann, *Mol. Cancer Res.*, 2012, **10**, 945–957.
39 J. Zhou, Y. Jiang, S. Hou, P. K. Upputuri, D. Wu, J. Li, P. Wang, X. Zhen, M. Pramanik, K. Pu and H. Duan, *ACS Nano*, 2018, **12**, 2643–2651.
40 J. Chen, S. Hou, Q. Liang, W. He, R. Li, H. Wang, Y. Zhu, B. Zhang, L. Chen, X. Dai, T. Zhang, J. Ren and H. Duan, *ACS Nano*, 2022, **16**, 2585–2597.
41 L. Huang, J. Xie, Q. Bi, Z. Li, S. Liu, Q. Shen and C. Li, *Mol. Pharm.*, 2017, **14**, 1742–1753.
42 L. J. Mah, A. El-Osta and T. C. Karagiannis, *Leukemia*, 2010, **24**, 679–686.
43 A. Kinner, W. Wu, C. Staudt and G. Iliakis, *Nucleic Acids Res.*, 2008, **36**, 5678–5694.
44 Y. Zhang, F. Huang, C. Ren, J. Liu, L. Yang, S. Chen, J. Chang, C. Yang, W. Wang, C. Zhang, Q. Liu, X. J. Liang and J. Liu, *Adv. Sci.*, 2019, **6**, 1801806.
45 G. Liang, X. Jin, S. Zhang and D. Xing, *Biomaterials*, 2017, **144**, 95–104.
46 C. Ganesh Kumar, Y. Poornachandra and C. Chandrasekhar, *Nanoscale*, 2018, **10**, 19639.
47 W. Roa, X. Zhang, L. Guo, A. Shaw, X. Hu, Y. Xiong, S. Gulavita, S. Patel, X. Sun, J. Chen, R. Moore and J. Z. Xing, *Nanotechnology*, 2009, **20**, 375101.
48 M. Payne, S. H. Bossmann and M. T. Basel, *Wiley Interdiscip. Rev.:Nanomed. Nanobiotechnol.*, 2020, **12**, e1638.
49 Z. Jiang, T. Li, H. Cheng, F. Zhang, X. Yang, S. Wang, J. Zhou and Y. Ding, *Asian J. Pharm. Sci.*, 2021, **16**, 738–761.
50 M. R. Horsman and J. Overgaard, *Clin. Oncol.*, 2007, **19**, 418–426.
51 J. A. Marteijn, H. Lans, W. Vermeulen and J. H. Hoeijmakers, *Nat. Rev. Mol. Cell Biol.*, 2014, **15**, 465–481.
52 D. Fantini, E. Moritz, F. Auvré, R. Amouroux, A. Campalans, B. Epe, A. Bravard and J. P. Radicella, *DNA Repair*, 2013, **12**, 227–237.
53 G. N. Castro, N. Cayado-Gutiérrez, F. C. Zoppino, M. A. Fanelli, F. D. Cuello-Carrión, M. Sottile, S. B. Nadin and D. R. Ciocca, *Cell Stress Chaperones*, 2015, **20**, 253–265.
54 T. Mantso, G. Goussetis, R. Franco, S. Botaitis, A. Pappa and M. Panayiotidis, *Semin. Cancer Biol.*, 2016, **37**, 96–105.
55 G. C. Terstappen, A. H. Meyer, R. D. Bell and W. Zhang, *Nat. Rev. Drug Discov.*, 2021, **20**, 362–383.
56 D. Wu, Q. Chen, X. Chen, F. Han, Z. Chen and Y. Wang, *Signal Transduct. Targeted Ther.*, 2023, **8**, 217.
57 S. Palma-Florez, A. López-Canosa, F. Moralez-Zavala, O. Castaño, M. J. Kogan, J. Samitier, A. Lagunas and M. Mir, *J. Nanobiotechnol.*, 2023, **21**, 115.
58 A. Xie, G. Cheng, J. Wu, Z. Li, G. Yu, X. Zhu and T. Chen, *Biomaterials*, 2025, **312**, 122749.
59 T. Xiao, M. He, F. Xu, Y. Fan, B. Jia, M. Shen, H. Wang and X. Shi, *ACS Nano*, 2021, **15**, 20377–20390.
60 G. Sonavane, K. Tomoda and K. Makino, *Colloids Surf., B*, 2008, **66**, 274–280.
61 W. H. De Jong, W. I. Hagens, P. Krystek, M. C. Burger, A. J. Sips and R. E. Geertsma, *Biomaterials*, 2008, **29**, 1912–1919.
62 M. Khongkow, T. Yata, S. Boonrungsiman, U. R. Ruktanonchai, D. Graham and K. Namdee, *Sci. Rep.*, 2019, **9**, 8278.